Ultrasonication-Assisted Synthesis of $Zn_xCd_{1-x}S$ for Enhanced Visible-Light Photocatalytic Activity

Lei Yang [1], Maolin Zhang [2] , Mingzhu Liu [1], You Fan [1], Haijie Ben [1,3], Longfeng Li [1,*] , Xianliang Fu [1] and Shifu Chen [1,*

[1] School of Chemistry and Materials Science, Huaibei Normal University, Huaibei 235000, China; yanglei225@hotmail.com (L.Y.); mzliu@chnu.edu.cn (M.L.); fanyou@tju.edu.cn (Y.F.); benhaijie@tju.edu.cn (H.B.); fuxiliang@chnu.edu.cn (X.F.)

[2] Department of Materials and Chemical Engineering, Bengbu University, Bengbu 233030, China; zhangml@chnu.edu.cn

[3] Key Laboratory of Pesticide & Chemical Biology of Ministry of Education, Institute of Environmental & Applied Chemistry, College of Chemistry, Central China Normal University, Wuhan 430079, China

* Correspondence: lilongfeng@chnu.edu.cn (L.L.); chshifu@chnu.edu.cn (S.C.); Tel.: +86-151-5552-2863 (L.L.); +86-139-6610-2728 (S.C.)

check for updates

Abstract: $Zn_xCd_{1-x}S$ as a solid solution photocatalyst has attracted widespread attention for its unique adjustable band gap structure and good and stable performance. A novel synthesis approach for $Zn_xCd_{1-x}S$ is still required to further improve its performance. In this study, we synthesized a series of $Zn_xCd_{1-x}S$ (x = 0−1) solid solutions via an ultrasonication-assisted hydrothermal route. In comparison with conventional methods of preparation, the sample prepared by our innovative method showed enhanced photocatalytic activity for the degradation of a methyl orange (MO) solution under visible light due to its high crystallinity and small crystallite size. Furthermore, the composition and bandgap of $Zn_xCd_{1-x}S$ can be tuned by adjusting the mole ratio of Zn^{2+}/Cd^{2+}. $Zn_{0.3}Cd_{0.7}S$ shows the highest level of activity and stability for the degradation of MO with k = 0.85 h^{-1}, which is 2.2 times higher than that of CdS. The balance between band gap structure-directed redox capacity and light absorption of $Zn_{0.3}Cd_{0.7}S$ accounts for its high photocatalytic performance, both of which are determined by the composition of the solid solution. Also, a degradation mechanism of MO over the sample is tentatively proposed. This study demonstrates a new strategy to synthesize highly efficient sulfide photocatalysts.

Keywords: $Zn_xCd_{1-x}S$ solid solution; tunable band structure; ultrasonication-assisted hydrothermal; photocatalysis; degradation of methyl orange

1. Introduction

Organic dyes discharged from the synthetic textile industry and other industrial processes are one of the largest groups of pollutants released into aquatic environments [1,2]. The removal of these dyes is vital not only for the protection and purification of water, but also for the maintenance of human and ecological health. Sunlight-driven heterogeneous photocatalysis is an ideal technique for the degradation of organic dyes in wastewater [3]. Almost 200 visible-light photocatalysts have been developed for the abatement of environmental pollutants and the extraction of H_2 from water [4–9]. Among them, CdS is regarded as a good candidate due to its reasonably narrow band gap (2.4 eV) for visible light absorption and high efficiency for the separation of charge carriers [9,10]. However, CdS instability due to self-photocorrosion by photogenerated holes (h^+) ($CdS + 2h^+ \rightarrow Cd^{2+} + S$) has restricted its use [9,11]. Thus, improving the stability of CdS emerges as a key issue for the application of CdS-based photocatalysis.

Some reasonable strategies, including modification with a cocatalyst, the construction of heterojunctions, and incorporation with other sulfides to form solid solutions, have been developed to improve the stability of CdS [12–19]. Among them, forming solid solutions offers a more straightforward and effective approach to manipulate the composition of CdS, and consequently, gives rise to the possibility of improving the photostability of the samples. Furthermore, the continuous adjustment of the band gap structure, i.e., not only the band gap energy but also the band edge position, can be achieved through the formation of a solid solution [11,20]. For example, the band structure of CdS and its photocatalytic performance can be tuned by the introduction of Zn^{2+} in the CdS lattice to form a $Zn_xCd_{1-x}S$ solid solution (ZCS). Compared to pristine CdS and ZnS, the activity and stability of ZCS can be optimized by changing the mole ratio of Zn^{2+}/Cd^{2+} [21–23]. The conduction band (CB) and valence band (VB) of the ZCS shift to more negative and positive positions, respectively, with the incorporation of Zn^{2+} into CdS [24,25]. It is well known that more negative conduction-band potential (E_{cb}) and more positive valence-band potential (E_{vb}) favor the formation of $^\bullet O_2{}^-$ and $^\bullet OH$, respectively [9,26–29]. These active oxygen species ($^\bullet O_2{}^-$ and $^\bullet OH$) play important roles in the photocatalytic degradation of dyes [28].

Various methods, such as hard-template [30,31], microwave [28], coprecipitation [23], solvothermal [20,32], and hydrothermal [29,33,34], have been developed for the preparation of ZCS. In general, the hydrothermal route is a green and cost-effective technique to prepare highly crystallized samples with fewer defects; however, it has drawbacks, e.g., it is difficult to regulate the particle size of the product, and it requires a long reaction time [9,29,33,35]. Thus for ZCS preparation, an optimized hydrothermal procedure to decrease particle size and treatment time is highly desirable.

An ultrasonication technique was employed to prepare various nanoparticles. This method not only promotes the dispersion of reactants and products, but also increases the rate of the reactions [12,36–38]. Some studies [12,36,38] have indicated that photocatalysts prepared via the ultrasonication-assisted technique showed much higher photocatalytic activities. With these considerations in mind, a combination of ultrasonication and hydrothermal treatment was used to prepare a series of ZCS solid solutions with a short reaction time. The photocatalytic performance of the samples was then assessed by the degradation of MO, a typical pollutant obtained in dye wastewater [9]. This study will describe a new strategy to synthesize highly efficient CdS-based photocatalysts in a short time.

2. Results and Discussion

2.1. Phase Structures and Morphology

The crystal structure and the average crystallite size of the prepared xZCS samples were analyzed by X-ray diffraction (XRD). As shown in Figure 1a, the diffraction peaks of CdS located at 24.8°, 26.4°, 28.2°, 43.7°, and 51.0° can be attributed to the (100), (002), (101), (110), and (112) planes of hexagonal CdS (JCPDF Card No. 06-0314), whereas the peaks of ZnS at 28.5°, 47.5°, and 56.2° can be ascribed to the (111), (220), and (311) of cubic ZnS (JCPDF Card No.05-0566). xZCS changes gradually from the hexagonal to the cubic phase with the gradual increase of Zn content. The incorporation of Zn atoms into the lattice of CdS influences the positions of Cd atoms, and subsequently changes the lattice structure of the ZCS. The gradual phase transition is thermodynamically favored by the fact that the zinc blende structure (cubic phase ZnS) is more stable than wurtzite, whereas the wurtzite phase is more stable for CdS [20]. Furthermore, the diffraction intensity of xZCS gradually decreases with an increase of Zn content, and the peaks shift toward a high diffraction angle (Figure 1b, i.e., the strongest peaks), corresponding to a gradual decrease of d-spacing value (Table 1). The changes indicated the formation of the xZCS [22,39,40]. A similar observation has been reported in Huang's work [41]. The differences in the cation radii of Zn^{2+} (0.74 Å) and Cd^{2+} (0.97 Å) are responsible for the successive peak shifts.
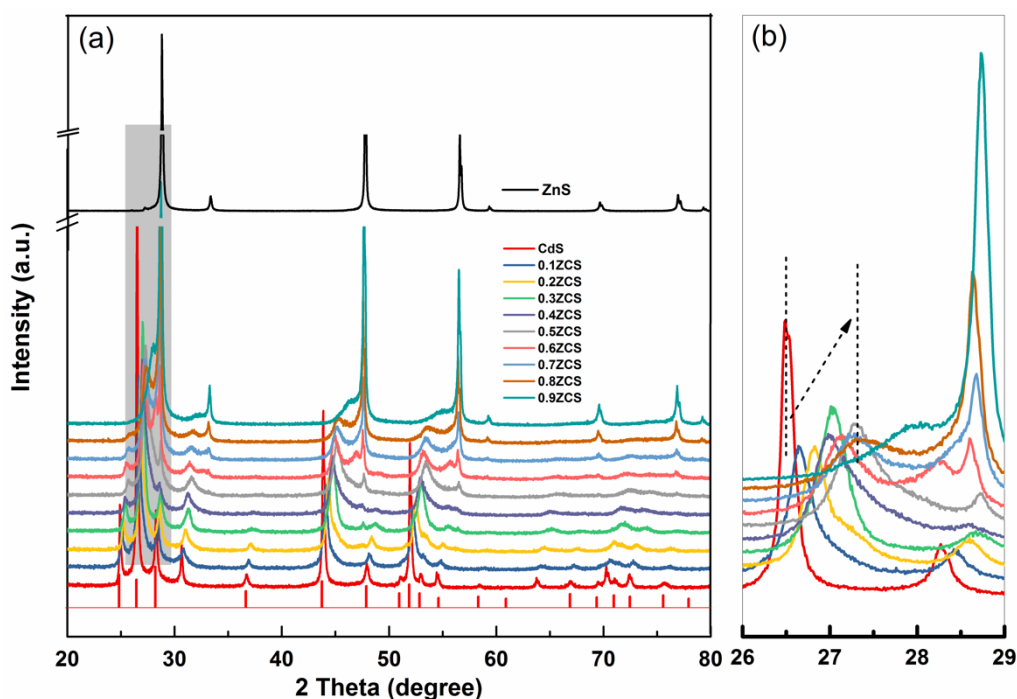
Figure 1. (**a**) XRD patterns of the prepared CdS, ZnS, and xZCS samples, (**b**) local enlarged patterns.

Table 1. Elemental composition and characterization results of the prepared samples.

Sample	Cd/Zn/S Molar Ratio	Size (nm)	Eg (eV)	d Value (Å)
CdS	$Zn_0Cd_{1.0}S$	28.45	2.15	3.36
0.1ZCS	$Zn_{0.1}Cd_{0.9}S$	21.70	2.19	3.34
0.2 ZCS	$Zn_{0.2}Cd_{0.8}S$	20.00	2.25	3.32
0.3 ZCS	$Zn_{0.3}Cd_{0.7}S$	14.50	2.28	3.30
0.4 ZCS	$Zn_{0.4}Cd_{0.6}S$	13.60	2.31	3.29
0.5 ZCS	$Zn_{0.5}Cd_{0.5}S$	13.10	2.35	3.28
0.6ZCS	$Zn_{0.6}Cd_{0.4}S$	12.93	2.37	3.26
0.7 ZCS	$Zn_{0.7}Cd_{0.3}S$	21.00	2.40	3.12
0.8 ZCS	$Zn_{0.8}Cd_{0.2}S$	28.64	2.45	3.11
0.9ZCS	$Zn_{0.9}Cd_{0.1}S$	28.96	3.28	3.10
ZnS	$Zn_{1.0}Cd_0S$	37.7	3.61	3.09

The crystallite size of the xZCS was calculated by the Scherrer equation. As shown in Table 1, the crystallite size first decreases from 28.45 to 12.93 nm, and then increases from 12.93 to 37.7 nm with the increase of Zn content. The obtained results are consistent with results of other studies [20,35].

The morphology and microstructure of the ZCS was further examined by transmission electron microscopy (TEM). As shown in Figure 2a, 0.3ZCS presents a nanosheet structure. The nanosheets are cumulative and the diameter of the aggregates is about 10–30 nm. The high-resolution transmission electron microscopy (HRTEM) image (Figure 2b) shows the interplanar spacing of 0.31 nm that corresponds to the (002) plane of hexagonal 0.3ZCS. The result is in agreement with that of XRD, as shown in Table 1.

2.2. X-ray Photoelectron Spectroscopy (XPS) Analysis

An XPS analysis was performed to identify the chemical composition of the 0.3ZCS. Due to its high photocatalytic degradation efficiency of methyl orange (MO) among all the samples, 0.3ZCS was chosen for XPS detection. The survey spectrum (Figure 3a) shows that the sample is composed of Zn, Cd, and S. High-resolution XPS spectra of Zn 2p (Figure 3b) and Cd 3d (Figure 3c) exhibit a pair of symmetrical peaks with the binding energy of 1021.4 eV (Zn 2p$_{3/2}$), 1044.5 eV (Zn 2p$_{1/2}$), 404.9

eV (Cd 3d$_{5/2}$), and 411.7 eV (Cd 3d$_{3/2}$), respectively, indicating that the valence states of Zn and Cd elements are +2 [32,42,43]. As seen in Figure 3d, S 2p peaks located at 161.44 eV (S 2p$_{3/2}$) and 162.64 (S 2p$_{1/2}$) confirm the presence of S^{2-} in 0.3ZCS [26,29,31]. In addition, the binding energy of Zn 2p and Cd 3d in 0.3ZCS is slightly higher than that of ZnS and CdS, respectively (Figure 3b,c), as also reported by other studies [39,44]. This can be attributed to the changed chemical states of the Zn and Cd atoms in 0.3ZCS [35]. The binding energy of S 2p in 0.3ZCS is slightly higher than that of CdS, but is close to to that of ZnS (Figure 3d). The shifts of the binding energies indicate the formation of a solid solution [29,39].
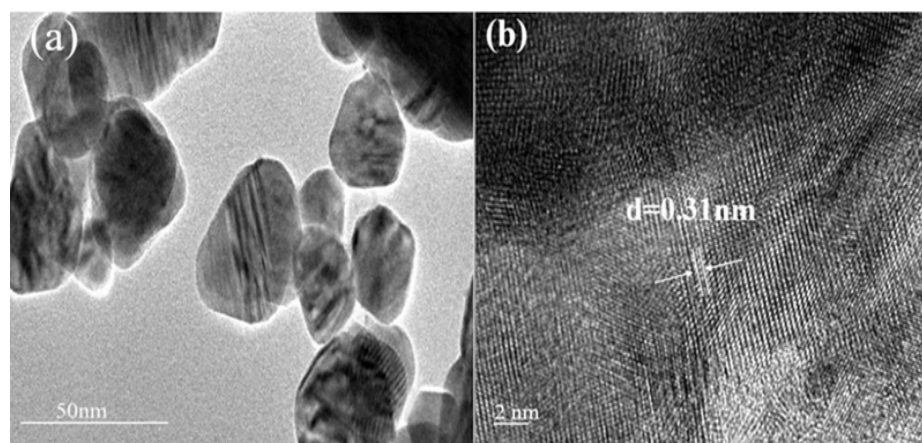

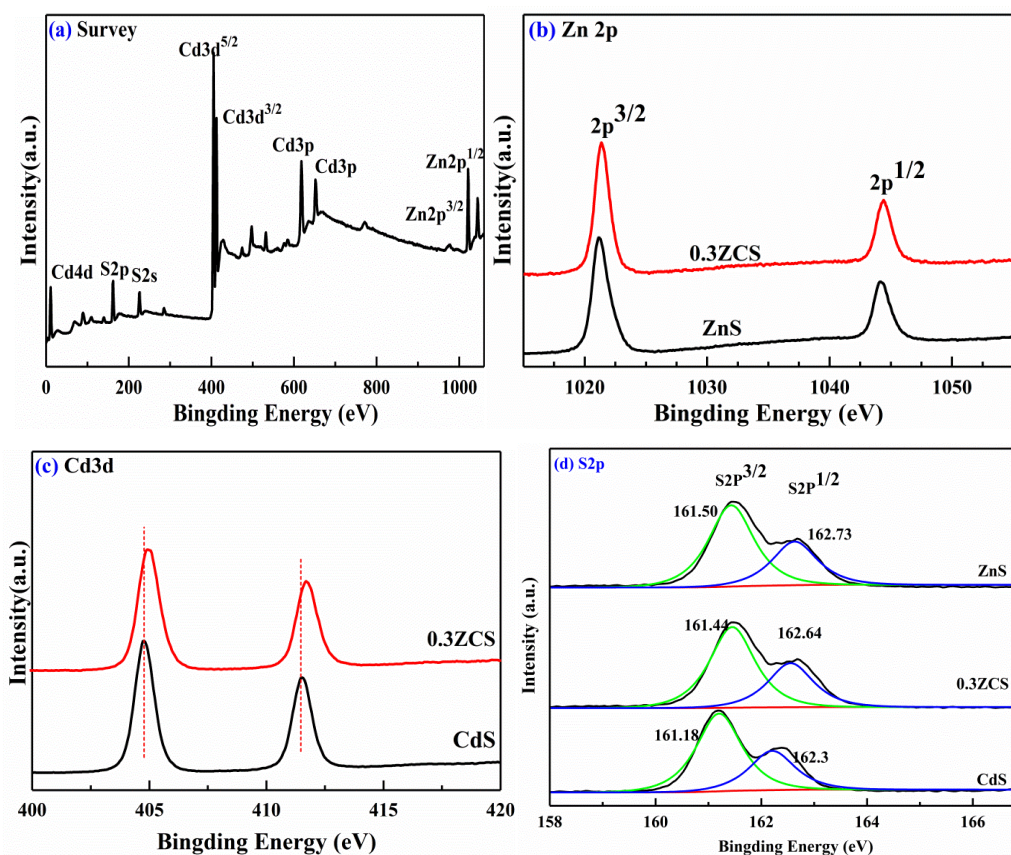**Figure 2.** (**a**) TEM and (**b**) HRTEM images of the 0.3ZCS sample.

Figure 3. (**a**) Survey and high resolution (**b**) Zn 2p; (**c**) Cd 3d; (**d**) S 2p XPS spectra of the prepared 0.3ZCS sample.

2.3. Optical Property and Band Structure Analysis

The UV-Vis diffuse reflectance spectroscopy (UV-Vis DRS) and the corresponding colors of the prepared xZCS samples are shown in Figure 4. With an increasing Zn content, the absorption edge of the prepared solid solution exhibits an obvious blue-shift from 576 to 343 nm, and the color of the sample changes gradually from dark orange to gray-white (inset of Figure 4).
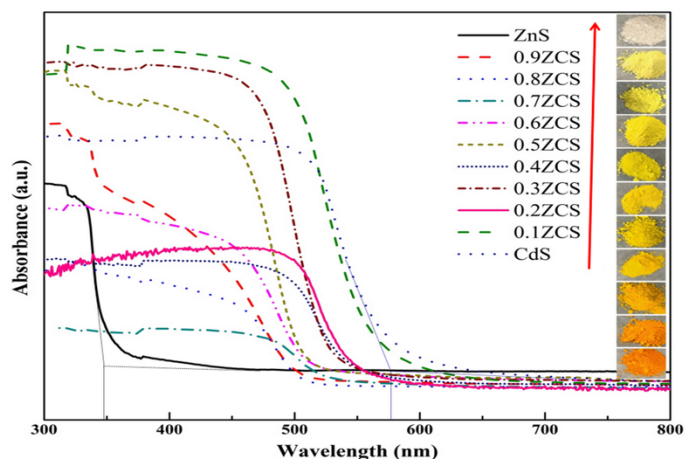

Figure 4. The UV-Vis DRS spectra of the $Zn_xCd_{1-x}S$ (x = 0–1.0) samples.

The band gap energy (E_g) values of the prepared ZCS samples are estimated by Equation (1), represented as follows:

$$E_g = 1240/\lambda \tag{1}$$

where λ is the absorption threshold. The results are summarized in Table 1. The E_g of the xZCS samples increases gradually from 2.15 to 3.61 eV with the increasing Zn content. This demonstrates that the intrinsic E_g of the ZCS can be regulated by changing the ratio of Zn:Cd [24,31,35].

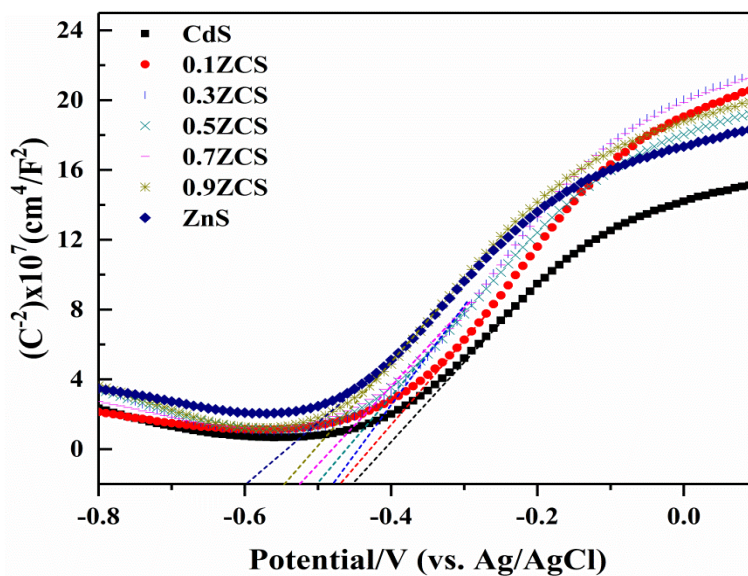A Mott–Schottky (M-S) measurement was further performed to determine the band structure of the ZCS samples (Figure 5).

Figure 5. Mott–Schottky plots of the prepared ZCS samples as electrode materials.

As shown in Figure 5, the positive slopes indicate that the xZCS samples are n-type semiconductors [32]. The flat-band potentials (E_{fb}) of the xZCS samples can be measured by

extrapolating the linear portion of the M-S curves to the X axis; the results are −0.45, −0.47, −0.48, −0.5, −0.52, −0.54, and −0.6 V (vs. Ag/AgCl) for CdS, 0.1ZCS, 0.3ZCS, 0.5ZCS, 0.7ZCS, 0.9ZCS, and ZnS, respectively. Generally, the E_{cb} of n-type semiconductor is more negative, i.e., about −0.1 or −0.2 V, compared to E_{fb} [32,45]. Thus, the E_{cb} of CdS, 0.1ZCS, 0.3ZCS, 0.5ZCS, 0.7ZCS, 0.9ZCS, and ZnS are −0.65, −0.67, −0.68, −0.7, −0.72, −0.74, and −0.8 V, respectively.

Based on the measured E_g and E_{cb} values, the E_{vb} of the prepared ZCS samples can be calculated by $E_{vb} = E_{cb} + E_g$. Then, the resulting E_{cb} and E_{vb} of the prepared ZCS samples are referred to as Normal Hydrogen Electrode Potential ($E_{NHE} = E_{Ag/AgCl} + 0.197$ V) [45]; the results are schematically illustrated in Figure 6.
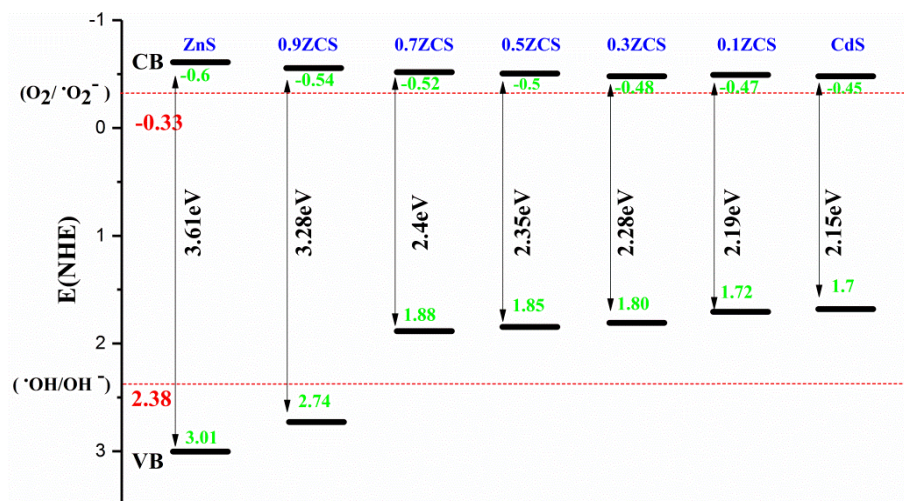

Figure 6. The conduction and valence band potentials of the prepared ZCS samples.

As shown in Figure 6, the E_{cb} of the ZCS samples are more negative than the standard redox potential of $O_2/{}^{\bullet}O_2^{-}$ (−0.33 V vs. NHE) [28], while the E_{vb} are less than the standard redox potential of ${}^{\bullet}OH/OH^{-}$ (2.38 V vs. NHE) [28]. A more negative E_{cb} enables the photogenerated electrons to reduce O_2 into ${}^{\bullet}O_2^{-}$ radicals, which can further induce the production of ${}^{\bullet}HO_2$ or ${}^{\bullet}OH$ radicals [26,27]. These active oxygen species (${}^{\bullet}O_2^{-}$, ${}^{\bullet}OH$, and ${}^{\bullet}HO_2$) can conduct photocatalytic degradation of the dyes [28]. On the other hand, although the E_{vb} of xZCS (excluding x = 0.9 and 1) is less than the standard redox potential of ${}^{\bullet}OH/OH^{-}$ and cannot oxidize OH^{-} to form ${}^{\bullet}OH$ radicals, the photogenerated holes can directly oxidize the dyes [26,28,29].

2.4. Photocatalytic Activity and Stability

The photocatalytic activity of the prepared xZCS was evaluated by the degradation of MO solution under visible light (λ > 420 nm). The variations of MO concentration with irradiation time are illustrated in Figure 7a. This indicated that the wide band gap ZnS shows no apparent activity for the decolorization of MO under visible light irradiation, whereas the ZCS samples show a monotonic decrease in the concentration of MO with irradiation time. Compared to pristine CdS, the introduction of Zn (x = from 0 to 0.3) into CdS crystal lattice forming ZCS solid solutions can substantially improve the photocatalytic activity. It was shown that 0.3ZCS yielded the best performance, that is, about 92% of MO was decolorized after irradiation for 3 h. Increasing the Zn content further from x = 0.3 to 0.9 leads to a decline of the activity.
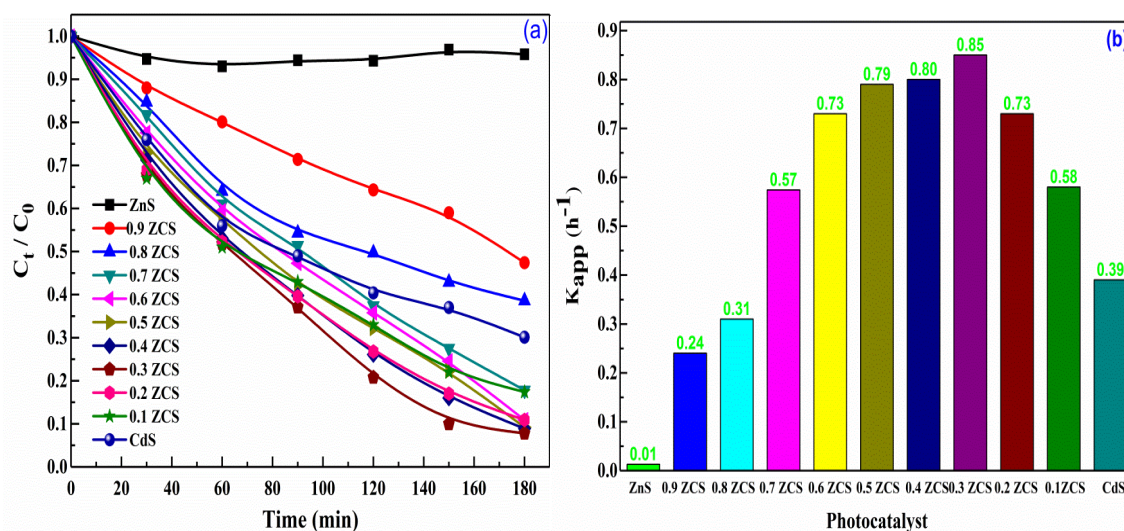
Figure 7. (**a**) Photocatalytic degradation of MO on the prepared xZCS samples; (**b**) K_{app} values of the prepared xZCS samples of the photocatalytic degradation of MO under visible light (> 420 nm) irradiation.

The degradation kinetic of MO over the prepared samples was further analyzed by a pseudo first-order kinetic Equation (2):

$$lnC_0/C_t = k_{app} \times t \qquad (2)$$

A model extensively used for the degradation of dyes was studied previously [6,46]. The resulting degradation rate constants (k_{app}) are summarized and compared in Figure 7b. Apparently, 0.3ZCS shows the highest degradation rate (0.85 h^{-1}), i.e., almost 2.2 times higher than that of CdS (0.39 h^{-1}). The superior photocatalytic performance of the 0.3ZCS sample for the degradation of the dyes was also reported in other studies [28,30,33]. In comparison, when using the same amount of the 0.3ZCS sample to degrade a MO solution of the same volume and concentration under the same test conditions, over 90% of the MO was decolorized after visible light irradiation for 3 h by the sample synthesized through the ultrasonic-assisted hydrothermal process, and after irradiation for no less than 5 h by the sample synthesized via traditional hydrothermal [33], microwave, and solvothermal routes [28], respectively. The best photocatalytic performance of 0.3ZCS prepared by our process may be attributed to its fabrication method as well as its proper composition, which offers a suitable band structure to strike a good balance between the light absorption and the redox capability of photoinduced charge carriers. The photocatalytic degradation mechanism is further discussed in the next paragraphs.

To investigate the stability of the prepared ZCS, five consecutive tests were carried out on the prepared 0.3ZCS sample.

As shown in Figure 8a, the high efficiency of 0.3ZCS still can be largely preserved after five consecutive tests. The slight drop of the performance was caused by the loss of the photocatalyst which occurred during the determination of MO concentration. The XRD results (Figure 8b) indicated that the spent 0.3ZCS after the five cycling tests shows an identical XRD pattern to the fresh one, further confirming the stability of the sample.
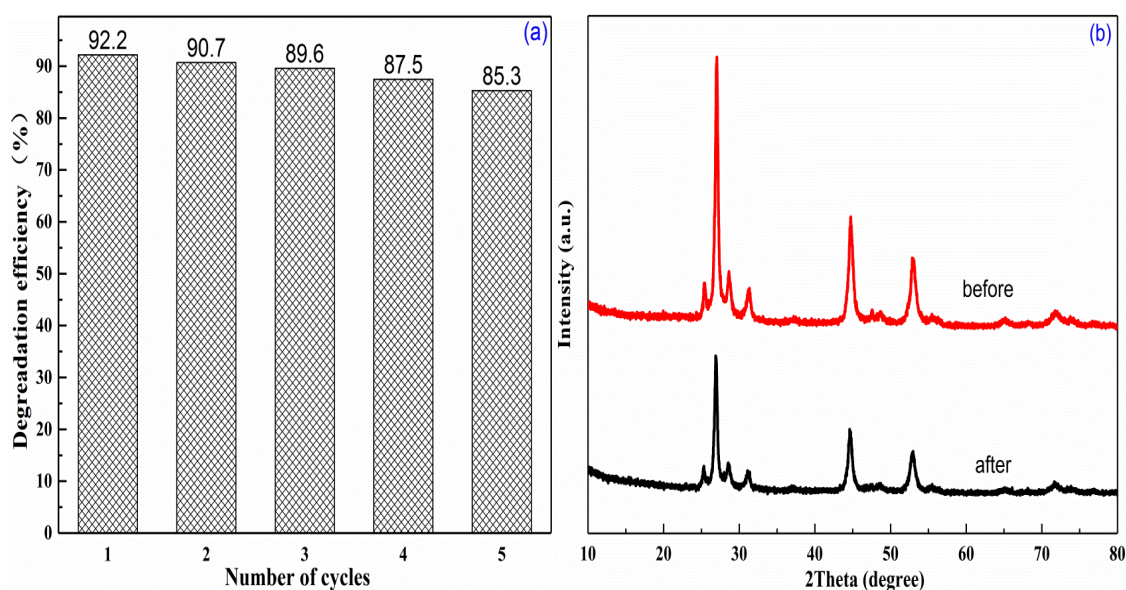
Figure 8. (**a**) Recycling tests for the photocatalytic degradation of MO over 0.3ZCS sample under visible light irradiation; (**b**) Comparison of XRD patterns of 0.3ZCS sample before and after five cycles tests.

2.5. Mechanism on Enhancement in Photocatalytic Activity

The absorption of light and the oxidation capability of the photoinduced charge carriers are key factors to determine the visible light photocatalytic degradation of dyes [33]. Generally, Cd-rich ZCS samples show better activity than Zn-rich samples because the former has a narrow band gap, and consequently, can generate more photoinduced charge carriers. However, a smaller band gap is not always better, because the redox capability of photo-generated charge carriers will decrease as the band gap becomes narrow. Therefore, to pursue a high photocatalytic performance of a solid solution photocatalyst, its composition needs to be optimized not only to maximize its visible light absorption range, but also to avoid a significant sacrifice of the redox capability of charge carriers. Our results indicate that x = 0.3−0.5 is the appropriate composition of ZCS, and 0.3ZCS shows the highest activity, which agrees well with the findings in previously reported works [28,30,33].

In addition, the fabrication method may also affect the photocatalytic activity of the photocatalysts. As mentioned above, compared with conventional hydrothermal, microwave, and solvothermal methods, a 0.3ZCS solid solution prepared by the ultrasonication-assisted hydrothermal process in this study has best photocatalytic performance. This is due to: (1) the ultrasonication treatment making the precursors mix well and react completely to form high-crystallinity crystals [35], and (2) once thioacetamide as a sulfur source combines with water to form H_2S gas, Zn^{2+} and Cd^{2+} quickly bind to the S^{2-} to form $Zn_xCd_{1-x}S$ nanoparticles, thus yielding improved photocatalytic activity [47].

3. Materials and Methods

3.1. Preparation of $Zn_xCd_{1-x}S$

All reagents were purchased from Sinopharm Chemical Reagent Co., Ltd (Shanghai, China). $Zn_xCd_{1-x}S$ was prepared by the following procedure. First, the reaction materials of $Zn(Ac)_2 \cdot 2H_2O$, $Cd(Ac)_2 \cdot 2H_2O$ (with different mole ratios as given in Table 1), and 0.94 g CH_3CSNH_2 were mixed in 40 mL of deionized water under ultrasonic vibration. Then, 10 mL of NaOH aqueous solution (4 mol·L^{-1}) was added dropwise into the above solution. After ultrasonic treatment for 0.5 h, the reaction mixture was transferred into a 100-mL, Teflon-lined, stainless-steel autoclave and then hydrothermally treated for 24 h at 180 °C. Next, the products were washed several times with deionized water and absolute ethanol, respectively, and dried in a vacuum oven for 8 h at 60 °C to obtain the final $Zn_xCd_{1-x}S$ samples.

Finally, according to the value of x in $Zn_xCd_{1-x}S$ (x = 0–1), the as-synthesized products were marked as xZCS, as exemplified in Table 1.

3.2. Photocatalytic Tests

The visible-light-responsive photocatalytic activities of the xZCS were evaluated by measuring the degradation rate of MO under visible light irradiation. For this, 0.04 g photocatalyst was dispersed in 80 mL of MO aqueous solution with an initial concentration of 20 mg·L^{-1} under magnetic stirring; then, the suspension was further stirred for 0.5 h in the dark to establish an adsorption–desorption equilibrium between the MO and the photocatalyst. Next, the suspension was exposed to visible-light irradiation from a 300 W xenon lamp (Beijing Zhongjiao Jinyuan Technology Co., Ltd, Beijing, China) equipped with a 420 nm cut-off filter for 3 h. At a given time interval, 5 mL suspension was taken out from the reaction solution and centrifuged to obtain a clear solution. The absorbance of MO was measured spectrophotometrically (722N visible spectrophotometer, Shanghai Precision & Scientific Instrument Co. Ltd. Shanghai, China) at its maximum absorption wavelength (463 nm). Finally, the photocatalytic degradation efficiency was estimated according to the time profiles of C_t/C_0; here, C_0 refers to the initial concentration of MO, and C_t corresponds to the concentration after irradiation for t min. The stability of the catalysts was evaluated by five cycles of photocatalytic degradation of MO.

3.3. Characterization

The crystal structure of the sample was determined by a Bruker D8 advance X-ray diffractometer (Bruker AXS, Karlsruhe, Germany) employing Cu Kα radiation (λ = 1.5406 Å) operated at 40 kV and 40 mA in air. The morphology and microstructure were analyzed by TEM and HRTEM using a JEOL JEM-2010 electron microscope (JEOL Ltd, Tokyo, Japan) with an acceleration voltage of 200 kV. The XPS measurements were conducted on an X-ray photoelectron spectrometer (ESCA LAB 250 Xi, Thermo Fisher Scientific, Waltham, MA, USA). The UV-Vis absorption spectra were recorded by UV-vis DRS (UV-3600, Shimadzu, Japan) with a wavelength range of 200–800 nm.

4. Conclusions

A series of ZCSs with nanosheet structures were successfully synthesized by an ultrasonication-assisted hydrothermal method. All the solid solutions (except for x = 0.8−1.0) showed enhanced efficiency for the photocatalytic degradation of MO solution under visible light irradiation in comparison with CdS; the highest degradation efficiency of 92% was achieved for $Zn_{0.3}Cd_{0.7}S$. The balance between the band gap structure-directed redox capacity and light absorption may open doors in the exploration of efficient photocatalysts with high stability.

Author Contributions: Conceptualization was done by L.Y., L.L., and S.C.; methodology was done by L.Y.; software analysis was performed by M.L. and X.F.; validation was done by M.Z. and Y.F.; formal analysis was done by H.B.; investigation was carried out by L.Y.; writing—original draft preparation was done by L.Y. and M.Z.; writing—review and editing was executed by L.L. and S.C.; visualization was done by M.Z. and Y.F.; supervision was done under L.L.; project administration was carried out by L.L. and S.C.; funding acquisition was done by L.L. and S.C. All authors have read and agreed to the published version of the manuscript.

Conflicts of Interest: The authors declare no conflict of interest.

References

1. Han, F.; Kambala, V.S.R.; Srinivasan, M.; Rajarathnam, D.; Naidu, R. Tailored titanium dioxide photocatalysts for the degradation of organic dyes in wastewater treatment: A review. *Appl. Catal. A Gen.* **2009**, *359*, 25–40. [CrossRef]

2.　Lam, S.M.; Sin, J.C.; Abdullah, A.Z.; Mohamed, A.R. Degradation of wastewaters containing organic dyes photocatalysed by zinc oxide: A review. *Desalin. Water Treat.* **2012**, *41*, 131–169. [CrossRef]

3.　Chong, M.N.; Jin, B.; Chow, C.W.; Saint, C. Recent developments in photocatalytic water treatment technology: A review. *Water Res.* **2010**, *44*, 2997–3027. [CrossRef] [PubMed]

4.　Abdulkarem, A.M.; Aref, A.A.; Abdulhabeeb, A.; Li, Y.F.; Yu, Y. Synthesis of Bi_2O_3/Cu_2O nanoflowers by hydrothermal method and its photocatalytic activity enhancement under simulated sunlight. *J. Alloys Compd.* **2013**, *560*, 132–141. [CrossRef]

5.　Yan, S.C.; Li, Z.S.; Zou, Z.G. Photodegradation performance of g-C_3N_4 fabricated by directly heating melamine. *Langmuir* **2009**, *25*, 10397–10401. [CrossRef] [PubMed]

6.　Zhang, M.L.; Yang, L.; Wang, Y.J.; Li, L.F.; Chen, S.F. High yield synthesis of homogeneous boron doping C_3N_4 nanocrystals with enhanced photocatalytic property. *Appl. Surf. Sci.* **2019**, *489*, 631–638. [CrossRef]

7.　Li, L.F.; Zhang, W.X.; Feng, C.; Luan, X.W.; Jiang, J.; Zhang, M.L. Preparation of nanocrystalline Cu_2O by a modified solid-state reaction method and its photocatalytic activity. *Mater. Lett.* **2013**, *107*, 123–125. [CrossRef]

8.　Zhang, Y.X.; Ye, Y.J.; Zhou, X.B.; Liu, Z.L.; Ma, D.; Li, B.; Liu, Q.H.; Zhu, G.P.; Chen, S.; Li, X. Facile preparation of a monodispersed CuO yolk-shelled structure with enhanced photochemical performance. *Cryst. Eng. Commun.* **2016**, *18*, 7994–8003. [CrossRef]

9.　Cheng, L.; Xiang, Q.J.; Liao, Y.L.; Zhang, H.W. CdS-Based photocatalysts. *Environ. Sci. Technol.* **2018**, *11*, 1362–1391. [CrossRef]

10.　Mort, J.; Spear, W.E. Hole drift mobility and lifetime in CdS crystals. *Phys. Rev. Lett.* **1962**, *8*, 314–315. [CrossRef]

11.　Deng, Q.; Miao, T.; Wang, Z.; Xu, Y.; Fu, X. Compositional regulation and modification of the host CdS for efficient photocatalytic hydrogen production: Case study on MoS_2 decorated $Co_{0.2}Cd_{0.8}S$ nanorods. *Chem. Eng. J.* **2019**, *378*, 122139. [CrossRef]

12.　Xie, Y.; Ali, G.; Yoo, S.H.; Cho, S.O. Sonication-assisted synthesis of CdS quantum-dot-sensitized TiO_2 nanotube arrays with enhanced photoelectrochemical and photocatalytic activity. *ACS Appl. Mater. Inter.* **2010**, *2*, 2910–2914. [CrossRef]

13.　Fu, J.; Chang, B.B.; Tian, Y.L.; Xi, F.N.; Dong, X.P. Novel C_3N_4-CdS composite photocatalysts with organic-inorganic heterojunctions: In situ synthesis, exceptional activity, high stability and photocatalytic mechanism. *J. Mater. Chem. A* **2013**, *1*, 3083–3090. [CrossRef]

14.　Lin, Y.F.; Hsu, Y.J. Interfacial charge carrier dynamics of type-II semiconductor nanoheterostructures. *Appl. Catal. B Environ.* **2013**, *130*, 93–98. [CrossRef]

15.　Ren, Z.; Zhang, J.; Xiao, F.X.; Xiao, G. Revisiting the construction of graphene–CdS nanocomposites as efficient visible-light-driven photocatalysts for selective organic transformation. *J. Mater. Chem. A* **2014**, *2*, 5330–5339. [CrossRef]

16.　Fan, Q.J.; Huang, Y.N.; Zhang, C.; Liu, J.J.; Piao, L.Y.; Yu, Y.C.; Zuo, S.L.; Li, B.S. Superior nanoporous graphitic carbon nitride photocatalyst coupled with CdS quantum dots for photodegradation of RhB. *Catal. Today* **2016**, *264*, 250–256. [CrossRef]

17.　Tian, Q.; Wu, W.; Liu, J.; Wu, Z.; Yao, W.; Ding, J.; Jiang, C. Dimensional heterostructures of 1D CdS/2D $ZnIn_2S_4$ composited with 2D graphene: Designed synthesis and superior photocatalytic performance. *Dalton Trans.* **2017**, *46*, 2770–2777. [CrossRef]

18.　Lai, J.; Qin, Y.M.; Lan, Y.; Zhang, C. GSH-assisted hydrothermal synthesis of $Mn_xCd_{1-x}S$ solid solution hollow spheres and their application in photocatalytic degradation. *Mat. Sci. Semicon. Proc.* **2016**, *52*, 82–90. [CrossRef]

19.　Swafford, L.A.; Weigand, L.A.; Bowers, M.J.; McBride, J.R.; Rapaport, J.L.; Watt, T.L.; Dixit, S.K.; Feldman, L.C.; Rosenthal, S.J. Homogeneously alloyed CdS_xSe_{1-x} nanocrystals: Synthesis, characterization, and composition/size-dependent band gap. *J. Am. Chem. Soc.* **2006**, *128*, 12299–12306. [CrossRef]

20.　Kaur, M.; Nagaraja, C.M. Template-free synthesis of $Zn_{1-x}Cd_xS$ nanocrystals with tunable band structure for efficient water splitting and reduction of nitroaromatics in water. *ACS Sustain. Chem. Eng.* **2017**, *5*, 4293–4303. [CrossRef]

21.　Zhao, X.; Luo, Z.; Hei, T.; Jiang, Y. One-pot synthesis of $Zn_xCd_{1-x}S$ nanoparticles with nano-twin structure. *J. Photochem. Photobiol. A* **2019**, *382*, 11919. [CrossRef]

22. Chen, J.; Lv, S.; Shen, Z.; Tian, P.; Chen, J.; Li, Y. Novel ZnCdS quantum dots engineering for enhanced visible-light-driven hydrogen evolution. *ACS Sustain. Chem. Eng.* **2019**, *7*, 13805–13814. [CrossRef]

23. Tang, L.; Kuai, L.; Li, Y.; Li, H.; Zhou, Y.; Zou, Z. $Zn_xCd_{1-x}S$ tunable band structure-directing photocatalytic activity and selectivity of visible-light reduction of CO_2 into liquid solar fuels. *Nanotechnology* **2018**, *29*, 064003. [CrossRef] [PubMed]

24. Lou, S.; Wang, W.; Jia, X.; Wang, Y.; Zhou, S. A unique nanoporous graphene-$Zn_xCd_{1-x}S$ hybrid nanocomposite for enhanced photocatalytic degradation of water pollutants. *Ceram. Int.* **2016**, *42*, 16775–16781. [CrossRef]

25. Yang, M.; Wang, Y.B.; Ren, Y.K.; Liu, E.Z.; Fan, J.; Hu, X.Y. Zn/Cd ratio-dependent synthetic conditions in ternary ZnCdS quantum dots. *J. Alloys Compd.* **2018**, *752*, 260–266. [CrossRef]

26. Wang, X.; Tian, H.; Cui, X.; Zheng, W.; Liu, Y. One-pot hydrothermal synthesis of mesoporous $Zn_xCd_{1-x}S$/reduced graphene oxide hybrid material and its enhanced photocatalytic activity. *Dalton Trans.* **2014**, *43*, 12894–12903. [CrossRef]

27. Li, W.; Li, D.; Xian, J.; Chen, W.; Hu, Y.; Shao, Y.; Fu, X. Specific analyses of the active species on $Zn_{0.28}Cd_{0.72}S$ and TiO_2 photocatalysts in the degradation of methyl orange. *J. Phys. Chem. C* **2010**, *114*, 21482–21492. [CrossRef]

28. Li, W.J.; Li, D.Z.; Zhang, W.J.; Hu, Y.; He, Y.H.; Fu, X.Z. Microwave synthesis of $Zn_xCd_{1-x}S$ nanorods and their photocatalytic activity under visible light. *J. Phys. Chem. C* **2010**, *114*, 2154–2159. [CrossRef]

29. Abideen, Z.U.; Teng, F. Effect of alkaline treatment on photochemical activity and stability of $Zn_{0.3}Cd_{0.7}S$. *Appl. Surf. Sci.* **2019**, *465*, 459–469. [CrossRef]

30. Lee, Y.Y.; Moon, J.H.; Choi, Y.S.; Park, G.O.; Jin, M.; Jin, L.Y.; Li, D.; Lee, J.Y.; Son, S.U.; Kim, J.M. Visible-light driven photocatalytic degradation of organic dyes over ordered mesoporous $Cd_xZn_{1-x}S$ materials. *J. Phys. Chem. C* **2017**, *121*, 5137–5144. [CrossRef]

31. Zhao, X.; Feng, J.; Liu, J.; Shi, W.; Yang, G.; Wang, G.C.; Cheng, P. An efficient, visible-light-driven, hydrogen evolution catalyst NiS/$Zn_xCd_{1-x}S$ nanocrystal derived from a metal-organic framework. *Angew. Chem. Int.* **2018**, *57*, 9790–9794. [CrossRef] [PubMed]

32. Liu, Y.; Wang, G.; Li, Y.; Jin, Z. 2D/1D $Zn_{0.7}Cd_{0.3}S$ p-n heterogeneous junction enhanced with $NiWO_4$ for efficient photocatalytic hydrogen evolution. *J. Colloid Interface Sci.* **2019**, *554*, 113–124. [CrossRef] [PubMed]

33. Li, W.; Li, D.; Chen, Z.; Huang, H.; Sun, M.; He, Y.; Fu, X. High-efficient degradation of dyes by $Zn_xCd_{1-x}S$ solid solutions under visible light irradiation. *J. Phys. Chem. C* **2008**, *112*, 14943–14947. [CrossRef]

34. Yu, J.; Yang, B.; Cheng, B. Noble-metal-free carbon nanotube-$Cd_{0.1}Zn_{0.9}S$ composites for high visible-light photocatalytic H_2-production performance. *Nanoscale* **2012**, *4*, 2670–2677. [CrossRef] [PubMed]

35. Li, Q.; Meng, H.; Zhou, P.; Zheng, Y.; Wang, J.; Yu, J.; Gong, J. $Zn_{1-x}Cd_xS$ solid solutions with controlled bandgap and enhanced visible-light photocatalytic H_2-production activity. *ACS Catal.* **2013**, *3*, 882–889. [CrossRef]

36. Pugazhenthiran, N.; Sathishkumar, P.; Murugesan, S.; Anandan, S. Effective degradation of acid orange 10 by catalytic ozonation in the presence of Au-Bi_2O_3 nanoparticles. *Chem. Eng. J.* **2011**, *168*, 1227–1233. [CrossRef]

37. Liao, K.H.; Lin, Y.S.; Macosko, C.W.; Haynes, C.L. Cytotoxicity of graphene oxide and graphene in human erythrocytes and skin fibroblasts. *ACS Appl. Mater. Inter.* **2011**, *3*, 2607–2615. [CrossRef]

38. Ghows, N.; Entezari, M.H. Exceptional catalytic efficiency in mineralization of the reactive textile azo dye (RB5) by a combination of ultrasound and core-shell nanoparticles (CdS/TiO_2). *J. Hazard. Mater.* **2011**, *195*, 132–138. [CrossRef]

39. Zhong, J.; Zhang, Y.; Hu, C.; Hou, R.; Yin, H.; Li, H.; Huo, Y. Supercritical solvothermal preparation of a $Zn_xCd_{1-x}S$ visible photocatalyst with enhanced activity. *J. Mater. Chem. A* **2014**, *2*, 19641–19647. [CrossRef]

40. Zhong, X.; Feng, Y.; Knoll, W.; Han, M. Alloyed $Zn_xCd_{1-x}S$ nanocrystals with highly narrow luminescence spectral width. *J. Am. Chem. Soc.* **2003**, *125*, 13559–13563. [CrossRef]

41. Huang, M.; Yu, J.; Deng, C.; Huang, Y.; Fan, M.; Li, B.; Tong, Z.; Zhang, F.; Dong, L. 3D nanospherical $Cd_xZn_{1-x}S$/reduced graphene oxide composites with superior photocatalytic activity and photocorrosion resistance. *Appl. Surf. Sci.* **2016**, *365*, 227–239. [CrossRef]

42. Wu, Y.J.; Yue, Z.K.; Liu, A.J.; Yang, P.; Zhu, M.S. P-type Cu-doped $Zn_{0.3}Cd_{0.7}S$/Graphene photocathode for efficient water splitting in a photoelectrochemical tandem cell. *ACS Sustain. Chem. Eng.* **2016**, *4*, 2569–2577. [CrossRef]

43.　Liu, Y.; Wang, G.R.; Ma, Y.L.; Jin, Z.L. Noble-metal-free visible light driven hetero-structural Ni/Zn$_x$Cd$_{1-x}$S photocatalyst for efficient hydrogen production. *Catal. Lett.* **2019**, *149*, 1788–1799. [CrossRef]

44.　Zhang, J.; Yu, J.; Jaroniec, M.; Gong, J.R. Noble metal-free reduced graphene oxide-Zn$_x$Cd$_{1-x}$S nanocomposite with enhanced solar photocatalytic H$_2$-production performance. *Nano Lett.* **2012**, *12*, 4584–4589. [CrossRef]

45.　Yi, S.S.; Yan, J.M.; Wulan, B.R.; Li, S.J.; Liu, K.H.; Jiang, Q. Noble-metal-free cobalt phosphide modified carbon nitride: An efficient photocatalyst for hydrogen generation. *Appl. Catal. B Environ.* **2017**, *200*, 477–483. [CrossRef]

46.　Wu, C.H.; Chang, H.W.; Chern, J.M. Basic dye decomposition kinetics in a photocatalytic slurry reactor. *J. Hazard. Mater.* **2006**, *137*, 336–343. [CrossRef]

47.　Wang, W.; Shen, H.; He, X.; Li, J. Effects of sulfur sources on properties of Cu$_2$ZnSnS$_4$ nanoparticles. *J. Nanopart. Res.* **2014**, *16*, 1–8. [CrossRef]